PNAS RESEARCH ARTICLE | CHEMISTRY

Tuning the electronic structure and SMSI by integrating trimetallic sites with defective ceria for the CO_2 reduction reaction

Charvi Singhvi[a], Gunjan Sharma[a], Rishi Verma[a], Vinod K. Paidi[b], Pieter Glatzel[b], Paul Paciok[c], Vashishtha B. Patel[d], Ojus Mohan[d], and Vivek Polshettiwar[a,1]

Affiliations are included on p. 11.

Edited by Charles T. Campbell, University of Washington, Seattle, WA; received June 11, 2024; accepted November 12, 2024 by Editorial Board Member Peter J. Rossky

Heterogeneous catalysts have emerged as a potential key for closing the carbon cycle by converting carbon dioxide (CO_2) into value-added chemicals. In this work, we report a highly active and stable ceria (CeO_2)-based electronically tuned trimetallic catalyst for CO_2 to CO conversion. A unique distribution of electron density between the defective ceria support and the trimetallic nanoparticles (of Ni, Cu, Zn) was established by creating the strong metal support interaction (SMSI) between them. The catalyst showed CO productivity of 49,279 mmol g^{-1} h^{-1} at 650 °C. CO selectivity up to 99% and excellent stability (rate remained unchanged even after 100 h) stemmed from the synergistic interactions among Ni-Cu-Zn sites and their SMSI with the defective ceria support. High-energy-resolution fluorescence-detection X-ray absorption spectroscopy (HERFD-XAS) confirmed this SMSI, further corroborated by in situ electron energy loss spectroscopy (EELS) and density functional theory (DFT) simulations. The in situ studies (HERFD-XAS & EELS) indicated the key role of oxygen vacancies of defective CeO_2 during catalysis. The in situ transmission electron microscopy (TEM) imaging under catalytic conditions visualized the movement and growth of active trimetallic sites, which completely stopped once SMSI was established. In situ FTIR (supported by DFT) provided a molecular-level understanding of the formation of various reaction intermediates and their conversion into products, which followed a complex coupling of direct dissociation and redox pathway assisted by hydrogen, simultaneously on different active sites. Thus, sophisticated manipulation of electronic properties of trimetallic sites and defect dynamics significantly enhanced catalytic performance during CO_2 to CO conversion.

CO_2 conversion | catalyst | defects | SMSI

Addressing the escalating concerns of climate change and carbon footprint reduction has catalyzed the scientific community's pursuit of innovative technologies. Among these, the development of heterogeneous catalysts stands out as a cornerstone for fostering a sustainable future (1–16). These catalysts hold the promise of closing the carbon cycle by enabling the conversion of carbon dioxide (CO_2) into value-added chemicals, by utilizing green hydrogen (1–16). Conversion of CO_2 into CO by the reverse water-gas shift reaction, an important C1-building block in large industrial processes like the Fischer–Tropsch hydrocarbon synthesis, the Monsanto/Cativa acetic acid synthesis, and higher alcohol syntheses, is considered to be one of the most promising ways to mitigate the CO_2 emissions (1–16). Despite the potential and strides made in this domain, the quest for optimal catalysts is hampered by challenges such as moderate catalytic activity, poor stability, coking, and loss of selectivity at high reaction temperatures, which made the processes unsustainable (1–16). These limitations underscore the imperative for breakthroughs in catalyst design and functionality for CO_2 reduction reaction (CO_2RR).

One way to achieve this is via the utilization of the phenomenon known as strong metal–support interactions (SMSIs), which enables the design of active nanocatalysts endowed with exceptional thermal stability, thus offering a viable solution to stability challenges in harsh reaction environments (17–24). SMSI, as reported by Tauster et al. (17, 18), is a phenomenon where the interaction between metal nanoparticles and the support material is strong enough to alter the electronic properties of the metal nanoparticles. Leveraging the SMSI effect also offers a distinct advantage in orchestrating charge transfer dynamics between the active metal and the support (25–27). The ability to fine-tune the magnitude and direction of this electron density transfer between the metal and support by precisely adjusting the strength of SMSIs presents an effective approach

Significance

The conversion of carbon dioxide (CO_2) to CO through catalytic processes is hailed as an effective strategy for transforming CO_2 into useful products. Using a unique approach to catalyst design by leveraging the concepts of defects and strong metal–support interaction (SMSI), we identified a Ni-Cu-Zn/CeO_2 catalyst with excellent performance. Same conventional ceria, same conventional metal sites—so why does this combination of trimetallic sites and defective ceria perform so dramatically? In situ transmission electron microscopy (TEM) and X-ray absorption spectroscopy (XAS) studies provided the insights into interaction dynamics and the unique electron density distribution between CeO_2, its defects, and the trimetallic nanoparticles. These findings offer a unique approach to catalyst design.

The authors declare no competing interest.

This article is a PNAS Direct Submission. C.T.C. is a guest editor invited by the Editorial Board.

[1] To whom correspondence may be addressed. Email: vivekpol@tifr.res.in.

This article contains supporting information online at https://www.pnas.org/lookup/suppl/doi:10.1073/pnas.2411406122/-/DCSupplemental.

for modulating the Fermi levels (28–32). This modulation fosters the creation of abundant electron-rich or deficient interfacial active sites, thereby exerting significant influence on the adsorption behavior of reactant molecules and intermediate species, consequently tuning catalytic activity and selectivity (8, 33, 34).

In this work, we synthesized a ceria-based electronically tuned trimetallic catalyst, for the CO_2 to CO conversion. The Ni–Cu–Zn/CeO_2 catalyst achieved a unique synergy through the strategic distribution of electron density among the defective ceria support and the trimetallic nanoparticles (NPs) composed of Ni, Cu, and Zn. The SMSI established between these active sites and the ceria support not only enhanced the catalyst's activity but also its stability, effectively mitigating issues such as sintering and coking at elevated temperatures. Our breakthrough was evidenced by the catalyst's unprecedented catalytic performance, achieving CO productivity of 49,279 mmol g^{-1} h^{-1} at 650 °C. CO selectivity up to 99% and excellent stability (rate remained unchanged even after 100 h on stream) at 550 °C were also achieved.

We then undertook a comprehensive series of studies to understand why this combination of trimetallic sites and defective ceria outperforms the reported catalysts (as the use of ceria as well as these metals, was already heavily investigated in the literature). The underlying mechanism was rigorously investigated using in situ transmission electron microscopy (TEM), in situ scanning TEM (STEM)-electron energy loss spectroscopy (EELS), in situ high-energy-resolution fluorescence-detection X-ray absorption near edge structure (HERFD-XANES) spectroscopy, revealing the crucial role of strong interactions between the trimetallic NPs and the CeO_2 surface. These studies illuminated the importance of oxygen vacancies in both CO_2 activation and coke combustion (35–38). In situ Fourier-transform infrared (FTIR) spectroscopy studies offered a deep molecular-level understanding of the dynamic formation and conversion of reaction intermediates over time and thus possible reaction pathways. Based on in situ FTIR and density functional theory (DFT) studies, a comprehensive CO_2 reduction mechanism that integrates both direct dissociation and a redox pathway, facilitated by hydrogen across various active sites was proposed.

Results and Discussion

Catalytic Performance of Ni–Cu–Zn/CeO_2 for CO_2 to CO Conversion. The Ni–Cu–Zn/CeO_2 catalyst along with other control catalysts i.e., the monometallic and bimetallic catalysts were evaluated for the CO_2 reduction reaction at 550 °C under 15 bar pressure, 1:1 CO_2/H_2 ratio, and 4,680 L g^{-1} h^{-1} gas hourly space velocity (GHSV) in a flow reactor (*SI Appendix*, Schemes S1 and S2). The trimetallic catalyst surpassed all its mono- and bimetallic counterparts in terms of CO productivity, selectivity, and stability (Fig. 1*A* and *SI Appendix*, Fig. S1). When tested at various temperatures and higher GHSV of 33,429 L g^{-1} h^{-1}, the monometallic and bimetallic catalysts showed much lower activity as compared to the Ni–Cu–Zn/CeO_2 (Fig. 1*B*). Metal loading optimization was conducted to achieve optimal weight percentages of Ni, Cu, and Zn on ceria support (*SI Appendix*, Fig. S2 and *Supplementary Note* 1). GHSV was then optimized for Ni–Cu–Zn/CeO_2 catalyst at 550 °C, and 15 bar, the GHSV of 33,429 L g^{-1} h^{-1} was found to be the best, with a CO productivity of 21,148 mmol g^{-1} h^{-1} with 99% selectivity (Fig. 1*C*). Using optimized GHSV, the catalytic performance was evaluated under different CO_2:H_2 ratios, and the CO productivity was found to be maximum at the 1:1 ratio (Fig. 1*D*). Following this, a pressure scan between 1 and 20 bar was conducted at 550 °C and a GHSV of 33,429 L g^{-1} h^{-1}. Productivity exhibited a rise with increasing pressure and at 15 bar, it showed excellent productivity of 21,148 mmol g^{-1} h^{-1} maintaining 99% CO selectivity (Fig. 1*E*). However, transitioning from 15 bar to 20 bar led to a decrease in selectivity; hence, we opted to continue with the pressure set at 15 bar. The catalyst was also tested at a higher temperature of 650 °C to evaluate its performance under harsh conditions. At 650 °C and 9,120 L g^{-1} h^{-1} GHSV, the catalyst showed even higher productivity of 49,279 mmol g^{-1} h^{-1} with 25% CO_2 conversion and slightly inferior selectivity of 97% (Fig. 1*F*). Upon decreasing GHSV to 480 L g^{-1} h^{-1}, 57% conversion was attained concurrently maintaining high CO productivity and selectivity (Fig. 1*F*). Considering the high energy input for 650 °C and loss in CO selectivity, the optimum temperature was considered to be 550 °C. To understand the role of ceria support, different versions of Ni–Cu–Zn trimetallic control catalysts were also prepared using commercial bulk and nanoceria supports, following the same experimental protocol. The catalytic activity of these catalysts was consistently lower than that of our synthesized CeO_2-based catalyst, indicating the important role of physicochemical properties of CeO_2 synthesized using our protocol (*SI Appendix*, Fig. S3).

To confirm that CO_2 was the sole carbon source, the control experiment without CO_2 was carried out, and no products (CO and CH_4) were detected. TGA of ceria support was also performed and no carbon impurity was detected which excludes any participation of such impurities in the CO productivity (*SI Appendix*, Fig. S4). The carbon balance was calculated to be 99% (Fig. 1*E*). This was further confirmed by conducting the CO_2RR using isotopically labeled $^{13}CO_2$ gas. Gas chromatography-mass spectrometry (GC-MS) analysis of the products showed a signal corresponding to ^{13}CO (m/z = 29) and $^{13}CH_4$ (m/z = 17) in the mass spectrum (*SI Appendix*, Fig. S5), further confirming that CO was produced from the CO_2 feed gas.

In regard to stability, the CO productivity rate (~20,941 mmol g^{-1} h^{-1}) remained unchanged, even after operating for 100 h continuously, at 550 °C and 15 bar pressure (Fig. 1*G*), with no occurrence of coke formation [based on Raman spectroscopy, thermogravimetric analysis, and carbon balance (*SI Appendix*, Figs. S6–S8 and *Supplementary Notes* 2 and 3)]. This excellent stability of the catalyst was attributed to the strong interaction between defective CeO_2 support and trimetallic active sites (discussed in-depth in the subsequent sections).

Structural Characterization of the Ni–Cu–Zn/CeO_2 Catalysts. High-angle annular dark-field scanning TEM (HAADF-STEM) and secondary electron images of Ni–Cu–Zn/CeO_2 revealed metal NPs, mostly 2 to 10 nm in diameter, with a mean diameter of 7.4 nm (Fig. 2 *A* and *B* and *SI Appendix*, Figs. S9–S11). The energy dispersive X-ray spectroscopy (EDX) elemental map and fast Fourier transform (FFT) patterns analysis showed that the metal NPs consisted of Ni, Cu, and Zn, with some Zn species also present outside of the metal nanoparticles on the ceria surface (Fig. 2 *B*–*G* and *SI Appendix*, Figs. S9 and S10 and *Supplementary Note* 4). The Ni:Cu:Zn atomic ratios in the catalyst were 3:1:0.7 based on EDX and inductively coupled plasma mass spectrometry (ICP-MS) data (*SI Appendix*, Table S1). The STEM-EDX line scan data provided a clear indication of the elemental distribution along a specific trajectory on the sample (Fig. 2 *H* and *I*). As seen in the line plot, Ni and Cu signals are consistently observed together, with the Zn signal also present wherever Ni and Cu are detected, albeit at lower concentrations, indicating homogeneous mixing of three metals (Fig. 2 *H* and *I*). The magnified version of the figure (*Inset* in Fig. 2) clearly showed a distinct Zn signal alongside Ni and Cu. The Zn signal (at 80 nm) for trimetallic nanoparticle had a count of 6, while Ce, in the vacuum region

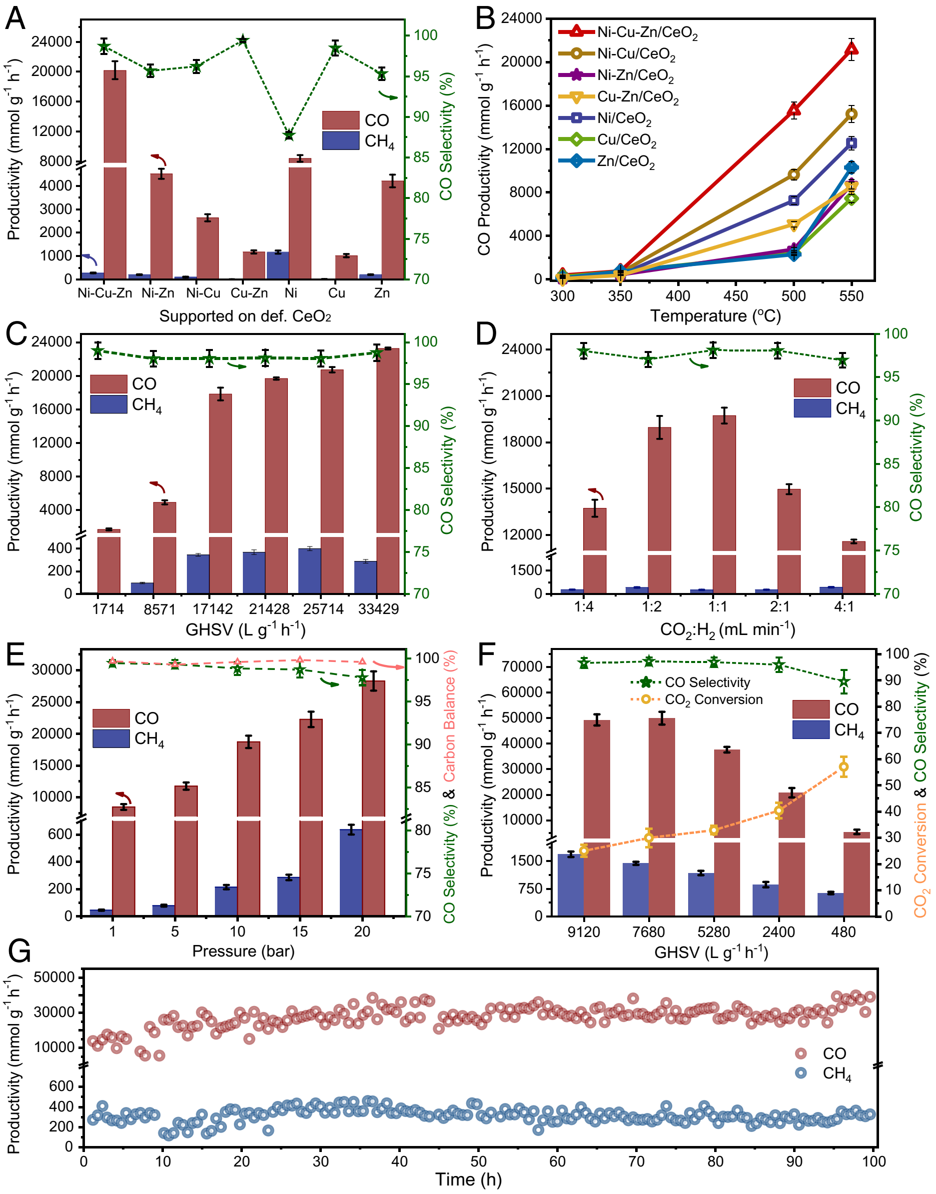

Fig. 1. Catalytic performance of Ni–Cu–Zn/CeO$_2$ catalyst for CO$_2$RR. Comparison of monometallic, bimetallic, and trimetallic catalysts at (*A*) 550 °C, 15 bar pressure, with 5 mg catalyst and 390 mL min^{-1} total flow (1:1 CO$_2$:H$_2$ ratio), i.e., 4,680 L g^{-1} h^{-1} GHSV, (*B*) various temperatures, 15 bar pressure, with 0.7 mg catalyst and 390 mL min^{-1} total flow (1:1 CO$_2$:H$_2$ ratio), i.e., 33,429 L g^{-1} h^{-1} GHSV; Effect of (*C*) GHSV (using 1:1 CO$_2$:H$_2$ ratio) and (*D*) CO$_2$/H$_2$ ratio (using 33,429 L g^{-1} h^{-1} GHSV), on CO productivity and selectivity, at 550 °C and 15 bar pressure; Effect of (*E*) Pressure at 550 °C using 33,429 L g^{-1} h^{-1} GHSV, and 1:1 CO$_2$/H$_2$ ratio on catalyst activity and selectivity; (*F*) CO$_2$ conversion at 650 °C, and 15 bar using 1:1 CO$_2$/H$_2$ ratio and various GHSVs; (*G*) Long-term catalyst stability for 100 h on stream at 550 °C and 15 bar using 33,429 L g^{-1} h^{-1} GHSV, and 1:1 CO$_2$/H$_2$ ratio.

(at 60 nm), showed a count close to 0, confirming that the Zn signal was not a background noise. While the Zn concentration was 0.7 wt% (counts ~ 6), part of it was distributed on the ceria surface, and the rest was incorporated into the trimetallic nanoparticle, leading to the observed lower counts relative to Ni (3 wt%, counts ~30) and Cu (1 wt%, counts ~12). To reconfirm this, we reran the EDX line map, which produced similar results (*SI Appendix*, Fig. S9 *C* and *D*). The electron microscopy images and EDX mapping of various control catalysts also showed good dispersion of metal NPs on the ceria and other supports (*SI Appendix*, Figs. S12–S21).

Mono- and bimetallic counterparts of the catalyst were also fully characterized by X-ray photoelectron spectroscopy (XPS), powder X-ray diffraction (PXRD), and N$_2$-sorption techniques. The surface area of the catalyst changes because of structural distortion upon defect creation (*SI Appendix*, Figs. S22–S26 and Table S2). Our synthesized Ni-Cu-Zn/CeO$_2$ exhibited a higher surface area and greater porosity, which contributed to the enhanced catalytic performance (*SI Appendix*, Figs. S3, S22, and S26 and *Supplementary Note* 5). These findings suggest that the superior performance of our catalyst can be attributed not only to the presence of oxygen vacancies but also to the optimized textural properties of the support. PXRD analysis of ceria support and catalysts showed a diffraction pattern similar to that of fluorite CeO$_2$, although the intensities were lower than those of pure CeO$_2$. This was due to distortion in the CeO$_2$ lattice on the creation of defects (*SI Appendix*, Figs. S27 and S28 and *Supplementary Note* 6).

To further elucidate the electronic structure and defect concentration within the catalysts, a high-resolution XPS analysis was performed, focusing on the Ce 3*d* region. The Ce 3*d* XPS indicated that the defect concentration or the Ce^{3+} phase increased in the following order among different catalysts: CeO$_2$< Cu-Zn/CeO$_2$ ~ Ni-Cu/CeO$_2$ < Ni-Zn/CeO$_2$ < Zn/CeO$_2$ ~ Ni-Cu-Zn/CeO$_2$ < Cu/CeO$_2$ < Ni/CeO$_2$ (*SI Appendix*, Figs. S29–S37 and *Supplementary Note* 7) as observed from the relative intensity of the peak at 918 eV. This indicated that an optimum concentration of defects was present in the trimetallic catalyst resulting in high activity. From Ni 2*p* XPS, the electron density on Ni sites in various catalysts was found to increase in the following order Ni-Zn/CeO$_2$ < Ni/CeO$_2$ < Ni-Cu-Zn/CeO$_2$ (*SI Appendix*, Figs. S30, S33, and S34) as observed from the increasing Ni^0 peaks. This indicated that the electron density on Ni sites increased slightly when Cu was present and decreased in the presence of Zn sites. The satellite peaks for Cu^{2+} were observed in the as-prepared sample at 963.4 eV which

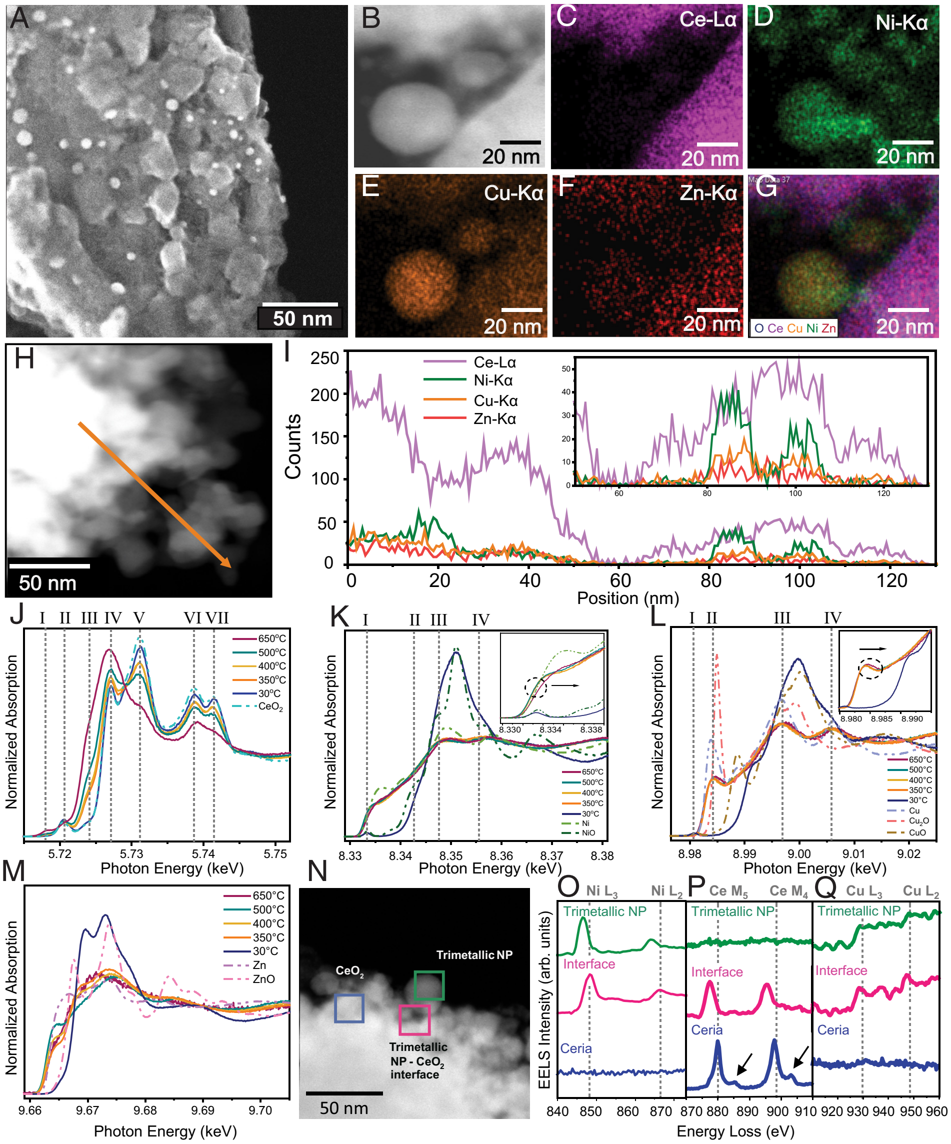

Fig. 2. Morphological and electronic characterization of the Ni-Cu-Zn/CeO_2 catalyst. (*A*) Secondary electron image, (*B*) HAADF-STEM image, (*C*–*G*) STEM-EDX element mapping; (*H*) STEM dark field image with an arrow indicating the EDX line scan position and (*I*) EDX line scan with Ce-Lα, Ni-Kα, Cu-Kα, and Zn-Kα signal of the reduced Ni-Cu-Zn/CeO_2 catalyst; in situ HERFD-XANES of as-prepared Ni–Cu–Zn/CeO_2 catalyst during in situ H_2 reduction conditions with 20 mL min^{-1} H_2 flow at various temperatures with a ramp of 20 °C min^{-1}, (*J*) Ce L_3-edge, (*K*) Ni K-edge, (*L*) Cu K-edge, and (*M*) Zn K-edge. In situ EELS of Ni–Cu–Zn/CeO_2 catalyst, (*N*) HAADF-STEM image where blue, pink, and green area denotes bulk CeO_2, trimetallic NP–CeO_2 interface, and trimetallic NP, respectively. In situ EELS spectra of different blue, pink, and green areas, (*O*) Ni $L_{2,3}$-edge, (*P*) Ce $M_{4,5}$-edge (arrows indicate small shoulders due to Ce^{4+} species) and (*Q*) Cu $L_{2,3}$-edge, under H_2 flow of 2.5 mL min^{-1} at 650 °C and 2.5 × 10^{-2} Pa.

disappeared as samples were reduced indicating the absence of Cu^{2+} sites in the catalyst (*SI Appendix*, Figs. S29–S32 and S35). The Zn 2*p* spectra suggested the presence of a small amount of ZnO in the catalyst, from the residual zinc species, which did not participate in the trimetallic nanoparticle formation and was present as oxide on the CeO_2 surface (*SI Appendix*, Figs. S29, S30, S32, and S33 and *Supplementary Note* 7). The trend in defect concentrations in all catalysts, as revealed by the Ce 3*d* XPS analysis, aligned with the observed PXRD patterns, reinforcing the relationship between lattice distortion and defect formation within the CeO_2 support across different catalysts.

To complement these findings and gain deeper insight into the catalyst's behavior, in situ STEM imaging was utilized to closely observe the dynamic processes occurring during the catalyst reduction step and under CO_2RR conditions, allowing for detailed real-time visualization of the formation, movement, and growth of active trimetallic sites. During the initial reduction stage, as temperatures reached 400 °C, trimetallic NPs formation was observed. At 500 °C, a noticeable growth in NPs size due to the aggregation and/or sintering of smaller nanoparticles was vividly captured in the supplementary in situ STEM (*SI Appendix*, Figs. S38–S43 and *Supplementary Note* 8, and in situ Movies S1 and S2). Intriguingly, upon reaching a higher temperature regime of 650 °C, the anticipated aggregation and sintering process of NPs did not occur (*SI Appendix*, Figs. S41 and S42, and in situ Movie S3). This phenomenon indicated the catalyst's transition into a state of strong metal–support interaction, which effectively halted further nanoparticle diffusion and sintering even at elevated temperatures. Further in situ STEM imaging performed under CO_2RR conditions, by flowing CO_2 and H_2 1:1 gaseous mixture at 500 °C (*SI Appendix*, Fig. S43 and in situ Movie S4), revealed that the trimetallic nanoparticles maintained their stability and positional integrity on the ceria support. This observation serves to reinforce the critical role of SMSI in ensuring the nanoparticles' resistance to the sintering process (*SI Appendix*, Figs. S44 and S45), for the development of efficient and long-lasting catalytic systems (39, 40). This prompted a deeper investigation into how these interactions between the nanoparticles and the ceria support evolve under reduction and reaction conditions.

Probing Defect Tuned SMSI by In Situ HERFD-XANES and In Situ STEM-EELS. The evolution of SMSI during the catalyst reduction step was studied by an in situ HERFD-XANES (*SI Appendix*, Scheme S3). The CeO_2 support in Ni-Cu-Zn/CeO_2 (as-prepared) exhibits fluorite structure (FCC) comprising solely Ce^{4+} sites (Fig. 2*J* and *SI Appendix*, *Supplementary Note* 9) (41–44). With increasing temperatures under reducing conditions (H_2 = 20 mL min^{-1}), a noticeable attenuation in spectral characteristics associated with

CeO_2 (II, V-VII) was observed, indicating the formation of Ce^{3+}. At 650 °C, the Ce^{3+} phase reached its highest concentration as evidenced by the increase in the intensity of the pre-edge feature I (5,718.2 eV). With increasing temperature under reducing conditions, a pronounced decline in peak intensity at feature V (5,731.0 eV) for Ce^{4+} was also observed (Fig. 2*J*). To understand the electronic structure of metal active sites and their role in tuning the SMSI, we then examined the Ni K-edge XANES spectra of Ni-Cu-Zn/CeO_2 (Fig. 2*K* and *SI Appendix, Supplementary Note* 9). Notably, the pre-edge peak intensity (feature I around 8,333 eV) was pronounced in standard NiO and the as-prepared sample, but diminished upon catalyst reduction. The absence of this feature indicated the presence of Ni in metallic form under reducing conditions from 350 °C to 650 °C (45–48). The XANES pre-edge positions, shown in the inset, fall between those of Ni foil and NiO, suggesting the presence of metallic Ni and Ni^{2+} (Fig. 2 *K*, *Inset*) which aligns with the Ni 2*p* XPS analysis (*SI Appendix*, Figs. S30, S33, and S34). However, a blue shift in the pre-edge region, feature I (8,333 eV), of the Ni K-edge compared to Ni foil at 650 °C was observed (Fig. 2 *K*, *Inset*). This shift attests to local distortions around Ni atoms and an augmented electron redistribution from Ni 4*s*/4*p* orbitals to the CeO_2 support, indicative of SMSI. A series of Cu K-edge XANES spectra were also recorded during the catalyst reduction step (Fig. 2*L* and *SI Appendix, Supplementary Note* 9). Feature I indicates the presence of the Cu^{2+} phase in the as-prepared catalyst (48, 49). However, upon introduction of a reducing H_2 gas, Cu^{2+} readily reduced at 350 °C. The XANES pre-edge positions of the reduced catalyst (area encircled in Fig. 2 *L*, *Inset*) lay between Cu foil and Cu_2O, suggesting the presence of a mixed state of Cu as also indicated by high-resolution XPS analysis of Cu K-edge (*SI Appendix*, Figs. S29–S32 and S35) (50–52). The feature II, in the sample reduced at 350 °C, 400 °C, and 500 °C, was observed at the energy of 8,943 eV. However, at 650 °C, there was a 0.9 eV shift toward higher energy, which indicated a higher partial positive charge being developed on Cu atoms (Fig. 2 *L*, *Inset*). This was due to the Cu site's interactions with defective ceria, forming partially oxidized Cu, which indicated the SMSI between defective ceria support and the Cu of the trimetallic NP. At 650 °C, feature III edge energy also shifted to higher energy by 1.1 eV (Fig. 2*L*), again indicating the partial positive charge being developed on Cu atoms at higher temperatures; a similar observation was also made for feature IV. In the case of Zn sites, as temperature increased from 350 °C to 650 °C the metallic Zn character increased (Fig. 2*M* and *SI Appendix, Supplementary Note* 9) (53, 54). Additionally, a shift in the edge-peak from 9,673.6 eV at 350 °C to 9,674.9 eV at 650 °C was observed which suggested the development of a partial positive charge due to strong interactions with ceria support. However, this was not observed in high-resolution XPS (*SI Appendix*, Fig. S30), where exposure to air during the measurements resulted in the complete oxidation of Zn, preventing the detection of metallic Zn in the analysis.

Although the HERFD-XANES experiment provided comprehensive insights into SMSI between active trimetallic sites and ceria defects, it primarily captured these interactions at a bulk level. To investigate the spatially resolved charge distribution and SMSI, we carried out an in situ STEM-EELS study. The STEM images of the catalyst revealed the presence of Ni-Cu-Zn trimetallic NPs anchored on the CeO_2 surface (Fig. 2 *N*–*Q*). The Ce $M_{4,5}$, Ni $L_{2,3}$, and Cu $L_{2,3}$ edges of Ni-Cu-Zn trimetallic NP alone, the metal NP–CeO_2 interface and ceria support alone were examined using EELS. The Ce $M_{4,5}$ edges revealed that the relative intensity (IM_5/IM_4) ratio of Ce $M_{4,5}$ edges decreased from 1.34 at the interface of trimetallic NP–CeO_2 to 1.12 on the CeO_2 alone, indicating the formation of Ce^{3+} species at the interface (Fig. 2 *N* and *P* and *SI Appendix*, Table S3 and *Supplementary Note* 10) (55–59). In addition, the bulk peaks of Ce have small shoulders compared to the interface at 885 and 902 eV, a signature of Ce^{4+} species (Fig. 2*P*) (55).

In the trimetallic NPs, the (IL_3/IL_2) ratio of Ni $L_{2,3}$ was 2.81 which decreased to 2.29 at the interface of trimetallic NP–CeO_2, indicating partial oxidation of the Ni site near the interface in comparison to Ni sites in the trimetallic nanoparticle alone (Fig. 2 *N* and *O* and *SI Appendix*, Table S3) (57, 58). For the Cu, in trimetallic NP alone, the Cu sites were in the reduced state i.e., Cu^0, while the trimetallic NP–CeO_2 interface was found to consist of partially oxidized Cu species, as evidenced by variations in the shape (as Cu^0 has a $3d^{10}$ electronic configuration, the intensities are incalculable) of the Cu $L_{2,3}$ edges (Fig. 2 *N* and *Q*) (58, 59). Thus, the change in the IL_3/IL_2 ratio in Ni, and, variations in the shapes of the $L_{2,3}$ edges in Cu in trimetallic nanoparticles supported on CeO_2 established the presence of the SMSI effect which induces the existence of Ni(II)–O, and Cu(I)–O oxidized states due to the interaction of metal atoms with the defects of CeO_{2-x} interface layer.

The STEM-EELS showed a mixture of metallic sites in reduced and partially oxidized forms that were strongly bonded with the defective CeO_2 surface, indicating the strong interactions via charge transfer from metal NPs and the CeO_2 surface. This effectively inhibited the growth and aggregation of nanoparticles during catalytic CO_2 reduction, resulting in stable catalysts. Notably, the trimetallic NP did not show any EELS signature of Ce M-edges, which indicated that there was no formation of a suboxide layer over the trimetallic NP surface (Fig. 2*P*) (which generally hinders the adsorption of reactant molecules) (60, 61). This ensured the availability of trimetallic sites for the adsorption of CO_2 and H_2 molecules followed by catalytic CO_2RR.

Thus, in situ EELS and in situ XANES analysis elucidated the interaction dynamics between CeO_2, its defects and the trimetallic NPs within the Ni-Cu-Zn/CeO_2 catalyst, revealing significant shifts in oxidation states and electron density distribution among the metal sites and ceria. These investigations emphasize the crucial role of electronic structure adjustments, facilitated through SMSI, in optimizing the catalyst's performance.

Comparison with Best Reported Catalytic Systems for CO_2RR. The performance of the Ni–Cu–Zn/CeO_2 catalyst was compared with the best-reported metal-based catalysts for CO_2 to CO conversion (27, 62–81). For CO_2 reduction, high catalytic activity is often achieved at the expense of selectivity and stability via triggering undesirable side reactions. Therefore, plotting selectivity versus productivity along with CO_2 conversion can be a good indication of overall performance. The pentagon plot in Fig. 3 compares various catalysts based on five key performance parameters, CO_2 conversion, temperature, GHSV, CO selectivity, and CO productivity (refer to *SI Appendix, Supplementary Note* 11 for details). Remarkably, Ni–Cu–Zn/CeO_2 demonstrated superior CO production rates, selectivity, conversion, and stability when compared to previously reported CO_2RR thermal catalysts (Fig. 3 and *SI Appendix*, Fig. S46-I and Table S4). Our catalyst exhibited a remarkable CO production rate of 49,279 mmol g^{-1} h^{-1} at 650 °C, representing a significant increase over the previous best-reported result (27, 62–81). Although this comparison is not perfect due to variations in experimental conditions used by various published reports, the difference in activity is enormous (ninefold). We also conducted a comparison using benchmark catalysts, tested under identical experimental setups and conditions. The results indicate that our developed catalyst outperforms the top four catalysts reported in the literature (*SI Appendix*, Fig. S46-II). A comprehensive comparison of the top 62 reported catalysts, including all pertinent experimental details has been provided in

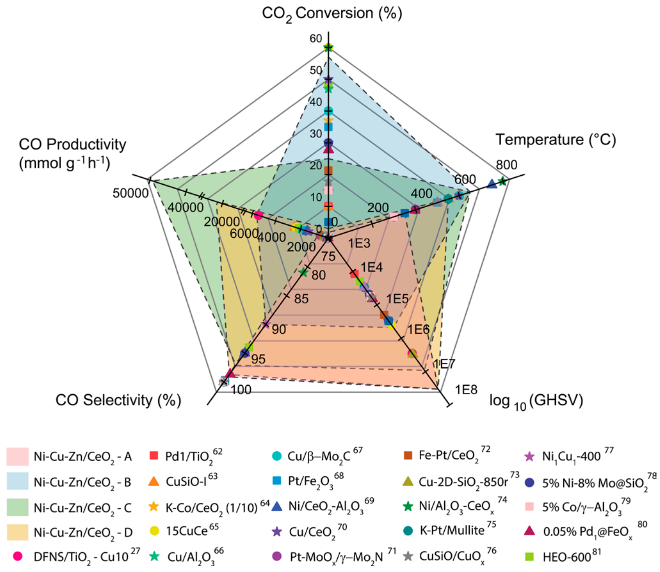

Fig. 3. Comparison (CO productivity, selectivity, CO$_2$ conversion, GHSV, reaction temperature, and catalyst stability) with the best-reported catalytic system for CO$_2$ to CO conversion where temperature & GHSV conditions were, (*A*) (Ni–Cu–Zn/CeO$_2$) 350 °C & 33,429 L g^{-1} h^{-1}, (*B*) (Ni–Cu–Zn/CeO$_2$) 650 °C & 480 L g^{-1} h^{-1}, (*C*) (Ni–Cu–Zn/CeO$_2$) 650 °C & 9,120 L g^{-1} h^{-1} and (*D*) (Ni–Cu–Zn/CeO$_2$) 550 °C & 33,429 L g^{-1} h^{-1}. A more detailed comparison is provided in *SI Appendix*, Table S4.

SI Appendix, Table S4. Thus, owing to the SMSI and electronic distribution as probed by XANES (Fig. 2 *J–M*) and STEM-EELS (Fig. 2 *N–Q*), the catalyst surpassed all other reported catalysts.

The Interplay of Oxygen Vacancies and Metal Sites in CO$_2$ Reduction Reaction. In previous sections, we observed how SMSI helped to improve the catalytic activity and stability to surpass other reported catalysts (Figs. 2 and 3). Oxygen vacancies are widely acknowledged as key sites for adsorbing and activating CO$_2$ and hence play a significant role in CO$_2$ reduction (27, 28, 35–38, 75). We tried to monitor how the electronic distribution was changing during the reaction by interaction with CO$_2$ and how the active sites were being regenerated in the process. The oxygen vacancies, metal sites, and interplay between them for the CO$_2$ activation step were investigated by in situ XANES and in situ STEM-EELS studies. Upon exposure to CO$_2$ at 650 °C, the oxygen vacancies in Ni–Cu–Zn/CeO$_2$ catalyst were occupied by the oxygen of CO$_2$ and hence there was an increase in XANES peak intensity corresponding to Ce^{4+} (Features II, IV–VII in Fig. 4*A*). However, when CO$_2$ and H$_2$ were simultaneously introduced at 650 °C, the amount of Ce^{3+} species increased in comparison to when only CO$_2$ was introduced, due to the simultaneous defect creation alongside CO$_2$ adsorption, particularly enhanced by metal-assisted H$_2$ spillover effects (Fig. 4 *A*, *Inset*) (27, 35–38). It was also evident when the catalyst was exposed with CO$_2$ + H$_2$ at 650 °C compared to 350 °C (*SI Appendix*, Fig. S47*A*), the Ce^{3+} concentration was higher at higher temperatures due to regeneration of O vacancies which were previously occupied by the oxygen atoms of CO$_2$ molecules. These continuous generation & regeneration of oxygen vacancies and Ce^{3+} centers during the progress of the reaction allowed the catalyst to remain active and stable even after 100 h.

We further studied this aspect by exploring the role of individual metal centers in the catalyst. In the case of Ni K-edge, the XANES pre-edge positions (area encircled, *SI Appendix*, Fig. S47*B*) lay close to Ni foil indicating that the Ni was in reduced form at all reaction temperatures (82). This suggested that both the processes of CO$_2$ adsorption and dissociation as well as H$_2$ dissociation were simultaneously happening, and in turn, the active Ni sites were being regenerated in the catalyst quickly. To confirm this, when only CO$_2$ was introduced (without H$_2$), CO$_2$ was strongly adsorbed on the Ni^0 sites and the oxidation state of Ni changed to +2 (Fig. 4*B*) (28, 83). Following this, when the catalyst was exposed to a reducing environment (only H$_2$), the Ni^{2+} sites were instantaneously reduced to Ni^0 (Fig. 4*B*). The evolution of CO$_2$ adsorbing on the Ni^0 sites was also studied by in situ XANES (*SI Appendix*, Fig. S48 and *Supplementary Note* 12). This study indicated the O vacancies in CeO$_2$ and Ni as key active sites for CO$_2$ adsorption.

The XANES pre-edge positions of the Cu K-edge of the catalyst at temperatures from 350 °C to 650 °C in the presence of the reaction mixture (CO$_2$ + H$_2$) lay between Cu foil and Cu$_2$O, indicating that their oxidation state was between 0 and +1 (Fig. 4*C* and *SI Appendix*, Fig. S47*C*) (83). Interestingly, when only CO$_2$ was introduced, there was no change observed in Cu K-edge spectra, indicating that CO$_2$ was not interacting strongly with Cu sites, however, Cu sites were actively dissociating H$_2$ (as indicated by the high concentration of defects formed by H$_2$ spillover in monometallic Cu/CeO$_2$, *SI Appendix*, Fig. S35 and XANES, discussed in the later section). This observation indicated that Cu sites did not act as CO$_2$ adsorption sites, unlike the Ni sites and rather only dissociated H$_2$ in a controlled way suppressing overhydrogenation to CH$_4$. To understand the role of Zn sites, Zn-K-edge was recorded in the presence of the reaction mixture. The edge-peak energy of Zn K-edge was highly blue shifted as shown in the encircled area (*SI Appendix*, Fig. S47*D*), indicating oxidation of Zn sites in the presence of CO$_2$ (15). Zn was oxidized to ZnO under the reaction conditions, as the CO$_2$ was absorbed at the Zn sites (Fig. 4*D*). This observation indicated that Zn sites promote CO$_2$ capture and activation. However, these sites were not actively dissociating H$_2$ resulting in CO$_2$-saturated Zn sites (52, 84). These results confirmed the strong interaction of CO$_2$ with Zn/ZnO sites resulting in their low desorption rate from the Ni–Cu–Zn/CeO$_2$ catalyst surface (Fig. 4*D*).

For a spatially resolved picture of these electronic density shifts, we further probed these XANES observations, by in situ STEM-EELS studies (*SI Appendix*, Scheme S4 and Fig. 4 *E–H*). In the case of the Ce M$_{4,5}$ edges, the relative intensity (IM$_5$/IM$_4$) ratio of Ce M$_{4,5}$ edges were 1.27 and 0.85, at the interface of metal NP–CeO$_2$ and in the CeO$_2$ alone, respectively, in the presence of CO$_2$ + H$_2$ mixture (Fig. 4 *F* and *H* and *SI Appendix*, Table S5) (85). In the trimetallic NP alone, the (IL$_3$/IL$_2$) ratio of Ni L$_{2,3}$ was 3.16, which decreased to 2.95 at the interface of trimetallic NP and CeO$_2$ implying the presence of partially oxidized Ni sites at the interface (Fig. 4*G* and *SI Appendix*, Table S5). For the Cu sites, as evidenced by variations in the shapes of the Cu L$_{2,3}$ edges, the trimetallic NP was found to be in the reduced state, while a partially oxidized Cu species was found at the NP–CeO$_2$ interface (Fig. 4*H* and *SI Appendix*, Table S5). The findings from this in situ EELS experiment were the persistence of the SMSI between the defective ceria support and the trimetallic nanoparticles even under reaction conditions which reduced the migration of NPs corroborating the observations from the in situ TEM studies (*SI Appendix*, Fig. S43 and Movie S4). The STEM-EELS spectra of the spent catalyst also showed signatures of oxidized metal sites at the interface of the trimetallic NP and CeO$_2$ indicating intact SMSI (*SI Appendix*, Fig. S49, Table S6, and *Supplementary Note* 13). Thus, the activity and stability of the catalyst were greatly enhanced due to the strong CO$_2$ activation ability of the trimetallic sites and the simultaneous formation and utilization of oxygen vacancies in CeO$_2$ support, which facilitated Mars–van Krevelen-type coke combustion (86, 87).

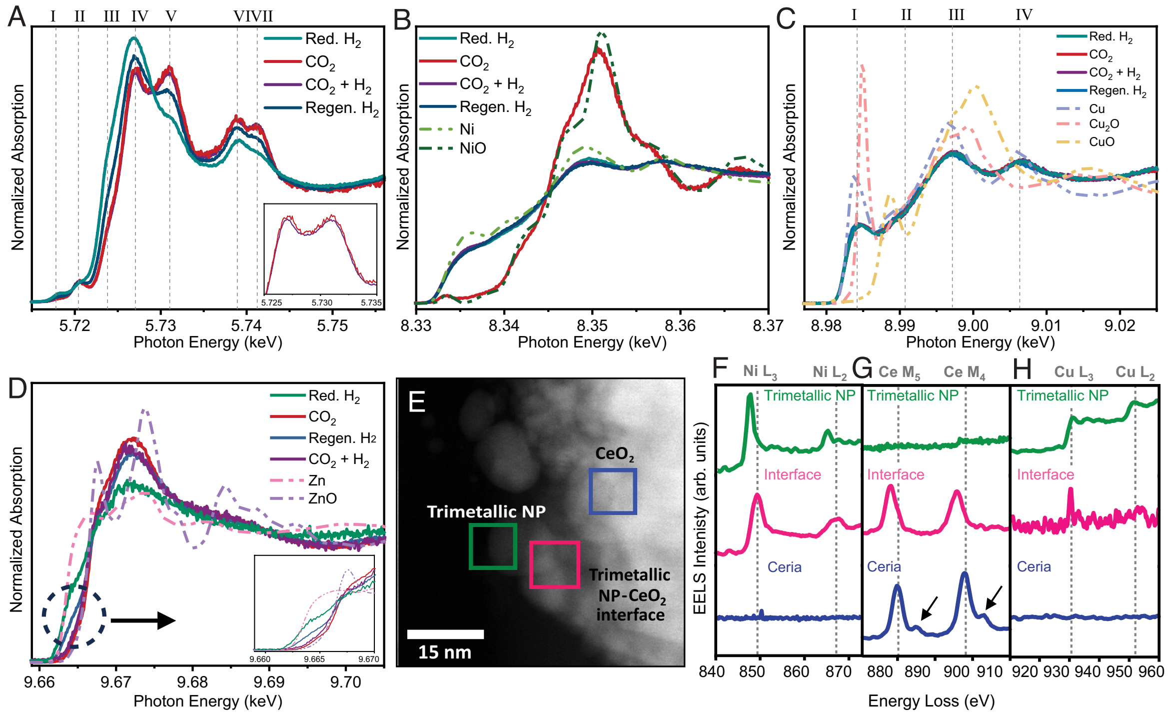

Fig. 4. Role of oxygen vacancies and trimetallic sites in CO_2RR. In situ HERFD-XANES studies of Ni-Cu-Zn/CeO_2 reduced sample under various conditions; only CO_2 (20 mL min^{-1}), reaction mixture of CO_2 + H_2 (10 mL min^{-1} each), and regeneration step using H_2 (20 mL min^{-1}), at 650 °C, (*A*) Ce L_3-edge, (*B*) Ni K-edge, (*C*) Cu K-edge, and (*D*) Zn K-edge; In situ STEM-EELS studies of Ni-Cu-Zn/CeO_2 reduced sample in presence of, CO_2 + H_2 with 1.2 mL min^{-1} flow each at 500 °C, (*E*) HAADF-STEM image and EELS spectra of (*F*) Ni $L_{2,3}$-edge, (*G*) Ce $M_{4,5}$-edge (arrows indicate small shoulders due to Ce^{4+} species), and (*H*) Cu $L_{2,3}$-edge where blue, pink, and green area denotes CeO_2, trimetallic NP–CeO_2 interface, and trimetallic NP alone, respectively.

Tuning the Electronic Structure of the Trimetallic Active Sites and Their Cooperativity with Defects. The previous discussions focused on how the unique electronic distribution was established at higher temperatures and preserved during the reaction. A major question still persisted about the role each metal component (Ni, Cu, and Zn) was playing to establish such a unique distribution and subsequently unprecedented high activity of the trimetallic catalyst as compared to the mono- and bimetallic counterparts (*SI Appendix*, Fig. S1). The Cu and Ni monometallic systems exhibited the highest defect concentrations, followed by similar levels in the Zn and Ni-Cu-Zn systems, despite this the latter demonstrated significantly higher CO productivity. It indicated that while defects were crucial for the formation of SMSI and could enhance catalytic properties, it was clear that other factors were also influencing the unique activity of the trimetallic system. In monometallic Ni/CeO_2, there was high defect concentration as well as the presence of multiple CO_2 activation sites, Ni and O vacancies. Although the Ni/CeO_2 catalyst showed a high initial CO_2 productivity, CO selectivity was compromised (87%), and rapid deactivation occurred within 5 to 6 h due to coke formation (*SI Appendix*, Fig. S8). On the other hand, monometallic Cu/CeO_2, despite actively dissociating H_2 and creating a high number of defects in the ceria support, was less effective at activating CO_2. This was because, in the Cu/CeO_2 system, the O vacancies were the only sites for CO_2 activation, leading to lower overall activity in Cu/CeO_2. The monometallic Zn/CeO_2 catalyst was stable but it showed low CO_2 conversion (*SI Appendix*, Fig. S1). On the other hand, Cu/CeO_2 showcased 100% CO selectivity but was less active for CO_2 conversion as compared to Ni/CeO_2 and Zn/CeO_2 (*SI Appendix*, Fig. S1). In the case of bimetallic sites also, interestingly, the initial conversion of CO_2 differed depending on the metal component in the following order: Ni-Zn > Ni-Cu > Zn >> Cu-Zn (*SI Appendix*, Fig. S1).

These results implied that Zn promoted CO_2 capture and activation and alloying with Ni enhanced the activity, while alloying with copper alone significantly reduced this ability. Therefore, alloying Zn with both Ni and Cu may have neutralized the negative effect of Cu, thereby promoting CO_2 conversion, while maintaining high selectivity and stability. This demonstrated that the trimetallic alloy structure Ni-Cu-Zn was essential for high catalytic performance.

To understand these individual contributions of Ni, Cu, and Zn in modulating the electronic attributes of the trimetallic NPs and associated SMSI, XANES spectra of both mono- and bimetallic configurations were analyzed. It was observed that the highest defect concentration was in monometallic ceria followed by trimetallic and bimetallic ceria (*SI Appendix*, Fig. S50). This indicated that an optimum defect concentration in the trimetallic system allowed for reaching a favorable balance between the concentration of defect sites and the strength of interactions between ceria and metal nanoparticles (88).

The Ni sites are known to favor CO_2 reduction to methane (CO_2RR) (89–91). However, decreased electron density on Ni sites is known to promote early CO desorption without further hydrogenation, enhancing CO selectivity (88–90). The Ni K-edge XANES spectra of control catalysts were also recorded to comprehend the effect of Cu and Zn on Ni sites (*SI Appendix*, Fig. S51 and *Supplementary Note* 14). For Ni K-edge, the white line intensity decreased from Ni-Zn/CeO_2 to Ni-Cu/CeO_2 which implies that the electron density on Ni sites decreased in the presence of Zn and increased in the presence of Cu. The white line feature III (8,996 eV) in the Cu-K edge spectrum in various catalysts revealed that the partial positive charge on Cu increases in the presence of Ni due to the transfer of electron density from Cu to Ni sites (*SI Appendix*, Fig. S52). Based on the pre-edge region of Zn K-edge XANES spectra of various control catalysts (area encircled *SI Appendix*,

Fig. S53 and *Supplementary Note* 14), the electron density on Zn sites increased drastically as Ni and Cu were introduced in the catalyst, again implying that Zn sites were extracting the electron density from Ni and Cu (*SI Appendix*, Fig. S53). These trends were also supported by DFT studies in the subsequent section.

In our Ni-Cu-Zn/CeO_2 catalyst design, Zn was introduced to modify the electronic structure, depleting electron density from Ni sites, resulting in partially positive Ni sites and thus increased CO selectivity. Cu sites were chosen for their high CO selectivity and ability to facilitate H_2 dissociation, aiding controlled H transport to Ni sites, thereby preventing further hydrogenation of CO. This electronic tuning was augmented by Zn metal sites and SMSI with defective ceria support, promoting preferential CO desorption from electron-deficient metal species surfaces. This highlighted the significant impact of electronic tuning among trimetallic sites and the SMSI effect on surface coordination, enhancing activity and selectivity. Thus, the HERFD-XANES data provided valuable insights into the spatial proximity and interactions between Ni, Cu, and Zn. The electron density distributions indicated a homogeneous mixing of Ni, Cu, and Zn.

Thus, factors influencing the unique activity of the trimetallic system were,

i) Metal Synergy: The trimetallic system benefits from synergistic effects between the three metals (Ni, Cu, and Zn) that were not present in the mono- and bimetallic systems. These interactions enhance the catalytic performance beyond what was explained by defects alone. The specific combination and distribution of metals in the trimetallic system led to more favorable reaction pathways or enhanced stability compared to individual metals or bimetallic combinations.

ii) Active Sites and Reaction Pathways: The presence of multiple metals creates a more diverse range of active sites, improving the overall catalytic efficiency. While defects can alone adsorb and activate CO_2, the conversion to CO through the redox pathway requires dissociated H_2. Monometallic Ni and Cu, although they have a high number of defects, do not achieve the same level of stabilized catalytic activity as the trimetallic system. This was because, monometallic Ni, while effective in CO_2 activation, has a strong affinity for CO, leading to a slower desorption rate. This can result in over hydrogenation of CO, forming CH_4 and reducing CO selectivity. On the other hand, monometallic Cu, despite actively dissociating H_2 and creating a high number of defects in the ceria support, was less effective at activating CO_2. In the Cu/CeO_2 system, the O vacancies or defects in CeO_2 were the only sites for CO_2 activation, leading to lower overall activity in Cu/CeO_2. The synergy among Ni, Cu, and Zn modifies and integrates the different reaction pathways, leading to increased CO productivity.

iii) Support Interaction: The interaction between the trimetallic nanoparticles and the CeO_2 support was optimized via SMSI to tune the selectivity, maximize catalytic activity, and stability, beyond what was observed in their mono- and bimetallic counterparts.

Molecular Mechanism of CO_2RR by In Situ FTIR Study. The conversion of CO_2 to CO can occur through two pathways: the redox mechanism and the direct dissociative mechanism (27–29, 91–95). To get insight into the molecular mechanism, intermediate formation, and reaction dynamics of the CO_2 reduction process over Ni-Cu-Zn/CeO_2 catalyst, a time-dependent in situ FTIR study was conducted in transmission mode (Fig. 5 *A* and *B*). When the reduced Ni-Cu-Zn/CeO_2 was exposed to CO_2, the C═O stretching vibrations of linearly bonded CO atop a Ni atom (Ni^0–CO) were observed at 2,075 cm^{-1} indicating the dissociative pathway (Fig. 5 *A* and *B*) (90, 96, 97). Additional band around 1,847 to 1,852 cm^{-1} was attributed to the CO stretching of CO_2 molecule adsorbed on oxygen vacancies, suggesting the role of defect sites in CO_2 activation which was also observed from the increase in Ce^{4+} signal in the XANES spectra (Fig. 4*A*) (37, 93–95).

The band at 1,454 cm^{-1} was attributed to the asymmetric stretching vibration ν_{as} (COO) of bicarbonates, while the broadband at 1,693 to 1,697 cm^{-1} was due to the CO stretch vibration of bicarbonates (28, 88). These suggest a parallel occurrence of redox mechanism, possibly for the CO_2 captured at the defect sites as they were also observed with defective CeO_2 (*SI Appendix*, Fig. S54 and *Supplementary Note* 15). This was further confirmed by the strong bands at 1,517 to 1,521 cm^{-1} and 1,997 cm^{-1}, attributed to the C-H stretching of formate species (Fig. 5 *A* and *B*) (70, 75). The presence of bicarbonate and formate species was observed even without supplying H_2. This can be due to the reaction between adsorbed CO_2 and residual surface hydroxyl species of the CeO_2 support (27).

When H_2 was introduced along with CO_2, C-O stretching bands around 2,182 and 2,105 cm^{-1} were observed for gaseous CO as the reaction progressed via the regeneration of surface defect sites (via redox mechanism) and Ni sites (via dissociative mechanism) (74, 90).The presence of the Ni^0-CO band without the presence of H_2 suggested a CO_2 dissociation pathway at the nickel sites (Fig. 5*A*), which was indicated by the charge depletion at Ni in the Ni K-edge in situ XANES in the presence of only CO_2 (Fig. 4*B* and *SI Appendix*, Fig. S48) (90). A highly dispersed Ni site in the trimetallic system, favored the formation of linearly bonded Ni^0–CO over strong multicoordinated Ni bonding to CO. This allowed efficient desorption and high CO productivity, in addition to good selectivity. Since the bicarbonates and formate peaks were also observed for defective CeO_2, we conclude that the defect sites favored the redox mechanism which was enhanced due to metal-assisted H_2 dissociation (Fig. 5*B*).

Thus, the in situ FTIR study provided information about the formation of various reaction intermediates and their conversion to products with reaction time (Fig. 5*A*), while the in situ XANES (Fig. 4), in situ TEM (*SI Appendix*, Figs. S38–S43 and Movie S4), and in situ STEM-EELS (Fig. 4) studies provided information about how defect sites were formed and interacted with reactants during CO_2RR (Figs. 2 and 4). Based on these observations, we have proposed a reaction mechanism for Ni-Cu-Zn/CeO_2 catalyzed CO_2RR, which followed the direct dissociation pathway-(a) (shown in red) and the redox pathway-(b) (shown in blue) (Fig. 5*C*). In pathway (a), we observed the direct dissociation of CO_2 on the Ni site in the trimetallic nanoparticle supported defective CeO_2. Following CO_2 adsorption in step II (a), the molecule directly dissociated into CO* and O* species in step III (a). CO could desorb, while the O species was hydrogenated to form water in a subsequent step involving H_2 adsorption, step IV (a). In pathway (b), first, the CO_2 molecule adsorbed onto CeO_2 defect sites (oxygen vacancy), while H_2 dissociated on Cu and Ni sites in the trimetallic nanoparticles, step II (b). Here, hydrogen-assisted CO_2 conversion via the COOH intermediate was considered. The adsorbed CO_2 then reacted with the terminal hydroxy of CeO_2 to produce unstable bicarbonate species in step III (b). Hydrogenation of the OH moiety, by dissociated H_2 on Cu or Ni sites in the trimetallic nanoparticles, followed by spillover on CeO_2, in adsorbed COOH leads to the formation of formate

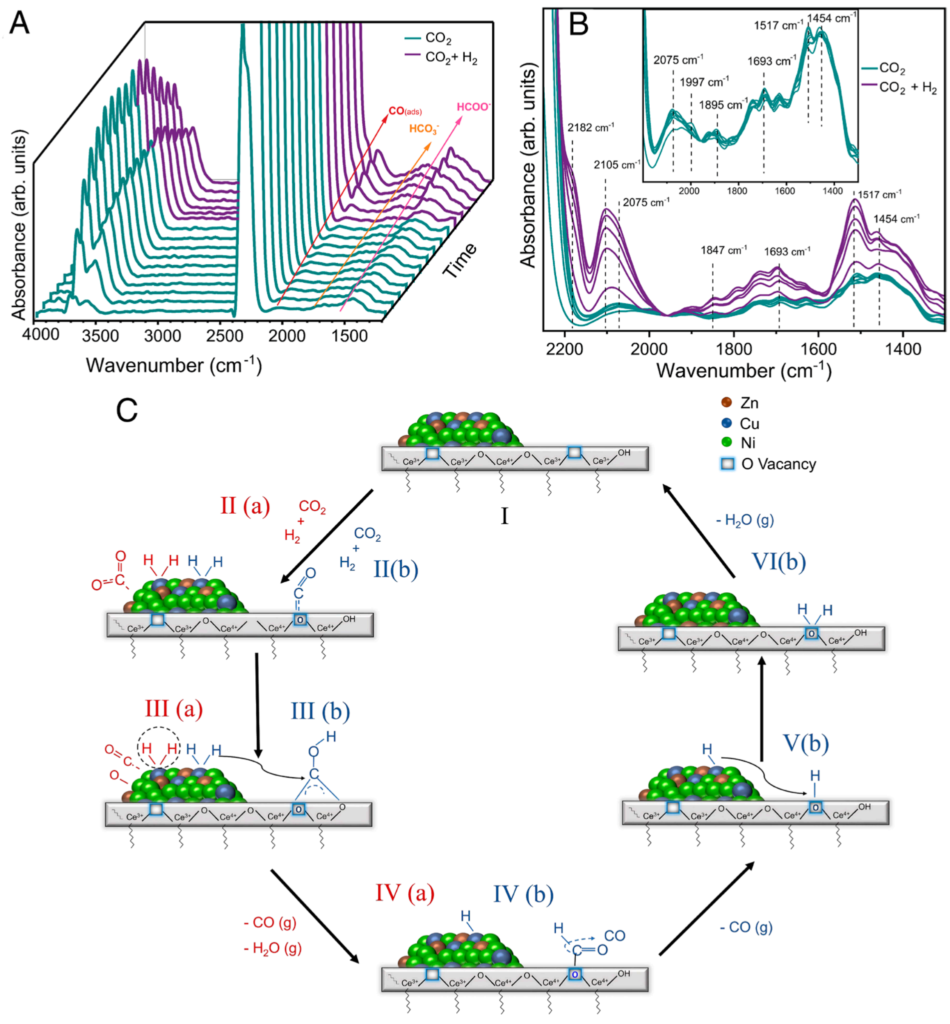

Fig. 5. In situ FTIR study for CO$_2$RR and formation of various reaction intermediates. (*A*) Time-dependent in situ FTIR spectra of Ni-Cu-Zn/CeO$_2$ catalyst during CO$_2$ and H$_2$ treatment at 550 °C; Enlarged view of the spectra while undergoing (*B*) CO$_2$ and CO$_2$ + H$_2$ treatment (the *Inset* corresponds to the band for CO during H$_2$ treatment); (*C*) Proposed reaction pathways for the CO$_2$ reduction to CO on Ni-Cu-Zn/CeO$_2$ catalyst. The direct dissociation pathway-(a) is shown in red and the redox pathway-(b) is shown in blue color.

species. In step IV (b) this formate intermediate readily breaks down into CO (gas) and OH (adsorbed) species. CO desorption took place in step V (b) and subsequently, in step VI (b) water was produced through the reaction of adsorbed H and OH species. After the desorption of this water molecule, the oxygen vacancy and Ce^{3+} sites were regenerated, to initiate a new redox cycle.

DFT Simulations to Understand SMSI and Reaction Mechanism. To get further insight into the adsorption energies of the intermediates and the activation energy for the CO$_2$ reduction reaction, DFT calculations were performed to validate the experimentally observed SMSI and reaction mechanism (*SI Appendix*, Figs. S55–S95, Tables S7–S9, and *Supplementary Note* 16–18 and Datasets S1–S41). The STEM-EDX analysis revealed that the elemental ratio of Ni:Cu:Zn in the synthesized catalyst was approximately 3:1:0.7. To closely match this experimental ratio, we developed a DFT model of the trimetallic site with a Ni:Cu:Zn ratio of 3.33:1:0.67, formulated as Ni$_{10}$Cu$_3$Zn$_2$. These models were chosen to accurately reflect the observed atomic composition. We employed this complex model to explore both the SMSI and the reaction mechanism. To understand the SMSI, we performed the Bader charge analysis of the ceria-supported trimetallic cluster and compared them with isolated Ni$_{15}$ and Ni$_{10}$Cu$_3$Zn$_2$ (*SI Appendix*, Fig. S55). The incorporation of the cluster on support led to charge exchange between them. This charge transfer between the cluster and the support was considered a key parameter to represent SMSI. The higher the exchange of charge between cluster and support, the stronger the metal–support interaction. The isolated monometallic and trimetallic clusters showed zero charges, as expected. However, when incorporated on the support, a net positive charge of 0.967 |e| and 0.954 |e| was observed on Ni$_{15}$ and Ni$_{10}$Cu$_3$Zn$_2$ clusters, respectively (*SI Appendix*, Table S7).

Interestingly, the metal atoms at the cluster–ceria interface attained partial positive charge, pulling the surface oxygen atoms toward them whereas the Zn atom in the bulk gained a negative charge of –0.002 from surrounded Ni atoms (Fig. 6 *A*–*D*). This coincides with the XANES (Figs. 2 and 4) and EELS (Fig. 2) analysis indicating SMSI which restricted diffusion and sintering of the cluster. The interaction between cluster atoms and surface oxygen weakened the cerium-oxygen bond, leading to charge transfer to the cerium atom. This stabilizes the Ce atom, possibly triggering defect formation on the surface (98). This explains the higher concentration of defects on monometallic ceria than on trimetallic ceria, as observed in the XANES (Fig. 2) and XPS (*SI Appendix*, Figs. S29–S37) studies.

Additionally, we studied the CO$_2$ conversion mechanism on the Ni-Cu-Zn trimetallic slab by exploring the direct dissociation and hydrogenation (formate and COOH*) pathways. Our DFT simulations showed that CO$_2$ preferred a direct dissociation with an activation barrier of 86.19 kJ mol^{-1} instead of its hydrogenation to HCOO* and COOH* which showed the activation barrier of 92.86 kJ mol^{-1} and 107.04 kJ mol^{-1} respectively (Fig. 6*E* and *SI Appendix*, Table S9). To understand the effect of different metal interfaces, we also considered the different metal atom combinations i.e., Ni-Ni, Ni-Cu, and Ni-Zn for CO$_2$ direct dissociation and hydrogenation pathways on respective surfaces (*SI Appendix*, Figs. S62–S71 and S76–S87). The Ni-Ni and Ni-Cu sites exhibited

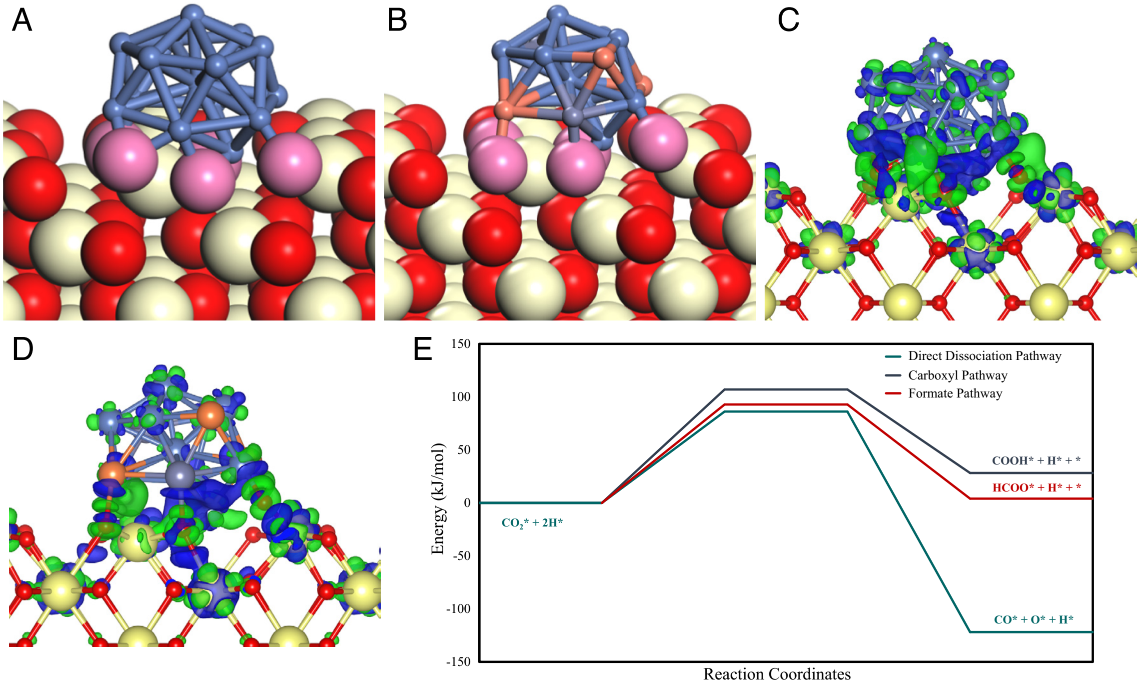

Fig. 6. Interface atoms interaction and reaction energy diagram. Interface oxygen atoms stretching toward metal cluster atoms showing partial oxidation of interface cluster metal atoms; (*A*) Side view of Ni_{15} on ceria, (*B*) Side view of $Ni_{15}Cu_3Zn_2$ on ceria; Electron density difference plots for (*C*) Ni and (*D*) $Ni_{15}Cu_3Zn_2$, on CeO_2 where green contours represent charge accumulations and blue contours denote charge depressions. The pink ball represents stretched oxygen atoms and the yellow, red, blue, orange, and black balls represent Ce, O, Ni, Cu, and Zn atoms, respectively; (*E*) The energy profile for CO_2 dissociation into CO and O on Ni-Cu-Zn.

almost similar activation barriers for direct dissociation of CO_2. However, the formation of HCOO* and COOH* observed a significantly larger difference of 20 kJ mol^{-1} in the activation barrier on these interfaces (*SI Appendix*, Figs. S76 and S77 and Table S9).

We also compared the CO_2 direct dissociation on Ni-Cu-Zn trimetallic surface with the CeO_2, monometallic Ni, Cu, and bimetallic Ni-Cu systems. CO_2 exhibited stronger bonding on the CeO_2 surface (binding energy of −109.8 kJ mol^{-1}) compared to the Ni-Cu-Zn slab (binding energy of −24 kJ mol^{-1}), possibly due to a strong CO_2—oxygen vacancy interaction on the reduced ceria surface (99). CO_2 dissociation on CeO_2 was highly endothermic (ΔE_{rxn} = 259.2 kJ mol^{-1}), suggesting that the activation barrier was even higher, posing a kinetic challenge for CO_2 dissociation on the ceria surface (97). In contrast, the activation barrier for CO_2 dissociation on the Ni-Cu-Zn trimetallic system was substantially lower at 86.19 kJ mol^{-1}. This notable difference in the activation barrier between Ni-Cu-Zn and CeO_2 (110) surfaces explains the higher CO_2 dissociation kinetics observed experimentally on the trimetallic cluster. Similarly, monometallic Cu showed a significantly higher activation barrier of 149.52 kJ mol^{-1}, which could be a reason for the poor performance of monometallic Cu. Contrary to this, direct dissociation of CO_2 on monometallic Ni and bimetallic Ni-Cu system reflected a lower activation barrier of 47.06 kJ mol^{-1} and 75.57 kJ mol^{-1}, respectively, indicating easier CO formation. These findings contradict the experimental observation of lower CO production rate on these surfaces (lowest on Ni-Cu surface at Ni-Ni interphase). To explain this discrepancy, we further investigated CO-binding energies on these catalyst surfaces.

Our DFT simulations revealed that CO binds more strongly on Ni and Ni-Cu surfaces than on Ni-Cu-Zn making CO desorption challenging on monometallic and bimetallic surfaces (*SI Appendix*, Table S8). It was observed that CO prefers the hollow sites on these surfaces (*SI Appendix*, Figs. S88–S95). However, when adsorbed at the hollow site of Ni, Cu, and Zn atom conjecture, CO migrated atop of Ni atom forming a Ni^0-CO bond as showcased by in situ FTIR analysis (*SI Appendix*, Fig. S80). This linear attachment reported a CO binding energy of −175.90 kJ mol^{-1}, the lowest among mono-, bi- and, trimetallic systems, indicating easier desorption of CO from the surface, thereby avoiding the subsequent reactions leading other C_1 product formation (*SI Appendix*, Figs. S88–S95 and Table S8). The higher CO production rate observed in experimental studies was attributed to this special synergy of Ni, Cu, and Zn elements in the catalytic system.

Conclusions

This work introduces an innovative ceria (CeO_2)-based, electronically tuned trimetallic catalyst for the efficient conversion of CO_2 to CO. The strategic incorporation of a trimetallic alloy comprising Ni, Cu, and Zn active sites, interfaced with defect-rich ceria supports harnessed SMSI and achieved an optimal distribution of electron density across the catalyst surface. The Ni-Cu-Zn/CeO_2 catalyst sets a new benchmark in CO_2 conversion efficiency exhibiting a CO production rate of 49,279 mmol g^{-1} h^{-1} at 650 °C. This performance was coupled with good CO selectivity and catalyst stability.

Through an array of sophisticated techniques including in situ EELS, and in situ XANES, a mechanistic insight into the formation and role of defect sites (Ce^{3+} and O-vacancies) in tuning SMSI was achieved. It revealed the interaction dynamics among CeO_2, its defects, and trimetallic NPs, showing notable shifts in oxidation states and electron density distribution. These investigations emphasized the essential role of electronic structure adjustments via SMSI in enhancing the catalyst's performance. In situ TEM imaging during catalytic conditions visualized real-time movement and growth of active trimetallic sites. Once SMSI was established, even at high temperatures, diffusion and sintering ceased completely.

The in situ FTIR study indicated a complex interplay between the direct dissociation of CO_2 to CO on Ni sites and the redox reduction pathway followed by CO_2 adsorbed on ceria O vacancies mediated by hydrogen. This intricate mechanism was facilitated by the distinct active sites present on the catalyst surface, highlighting the nuanced interaction between multimetallic systems and defect sites. Alloying Ni with Cu enhanced the CO selectivity and stability due to the ensemble effect while doped Zn species promoted CO_2 adsorption and activation while tuning electron density on Ni sites. The incorporation of Cu and Zn also helped in tuning the electron density on Ni enhancing the preferential CO desorption which was further corroborated by DFT studies. The O atoms oxidize the eliminated hydrogen to form H_2O or combust coke on the alloy surface or neighboring CeO_2 sites.

Thus, the unique symphony between the defective ceria support and the trimetallic nanoparticles fosters an environment conducive to enhanced catalytic performance.

Experimental and Computational Details. Experimental details for the synthesis of various catalysts, their characterizations, SEM, TEM, PXRD, XPS, N_2 sorption, TGA, Raman, in situ (XANES, EELS, and FTIR) studies, and catalytic CO_2 reduction are provided in *SI Appendix*. All the periodic DFT simulations were performed in the Vienna Ab initio simulation package and details are provided in *SI Appendix*.

Data, Materials, and Software Availability. Information includes experimental details for the synthesis of catalysts, catalysts characterizations, in-situ studies, catalysis experimental, reactor schematic, computational details, and structural coordinates of different models [*SI Appendix*, Schemes S1–S4, Figs. S1–S95, *Supplementary Notes* 1–18 and Tables S1–S9, DFT Coordinates file (Datasets S1–S41) and in situ Movies S1–S4]. All study data are included in the article and/or supporting information.

ACKNOWLEDGMENTS. We acknowledge the funding support of the Department of Atomic Energy, Government of India, project no. 12-R&D-TFR-RTI4003. We acknowledge the EM and XRD facility of Tata Institute of Fundamental Research, Mumbai, and European Synchrotron Radiation Facility, Grenoble for HERFD-XANES. O.M. acknowledges the new faculty seed grant from Indian Institute of Technology, Bombay: RD/0522-IRCCSH0-012 and the National Supercomputing Mission for providing computing resources of "PARAM Siddhi-AI." This work contains results obtained from the experiments performed at the Ernst Ruska-Centre (ER-C) for Microscopy and Spectroscopy with Electrons at the Forschungszentrum Jülich in Germany. The ER-C beam-time access was provided via the Transnational Access in the frame of ReMade-at-ARI Project [PID 25919] funded by the European Union as part of the Horizon Europe call HORIZON-INFRA-2021-SERV-01 under grant agreement number 101058414 and cofunded by UK Research and Innovation under the UK government's Horizon Europe funding guarantee (grant number 10039728) and by the Swiss State Secretariat for Education, Research and Innovation (SERI) under contract number 22.00187. Views and opinions expressed are however those of the author(s) only and do not necessarily reflect those of the European Union or the UK Science and Technology Facilities Council or the Swiss State SERI. Neither the European Union nor the granting authorities can be held responsible for them.

Author affiliations: [a]Department of Chemical Sciences, Tata Institute of Fundamental Research, Mumbai 400005, India; [b]Experiments Division, European Synchrotron Radiation Facility, Grenoble 38043, Cedex 9, France; [c]Ernst-Ruska Center for Microscopy and Spectroscopy with Electrons, Forschungszentrum Jülich, Jülich 52425, Germany; and [d]Department of Chemical Engineering, Indian Institute of Technology Bombay, Mumbai 400076, India

Author contributions: V.P. proposed the research direction, designed the project, and guided the project; V.P., C.S., G.S., and R.V. designed various experiments; C.S. performed the experiments (synthesis, characterizations, catalysis); G.S. and R.V. performed in-situ FTIR studies and defect characterization studies; V.P. and P.P. performed in-situ TEM and EELS studies; C.S., G.S., V.P., V.K.P., and P.G. performed XAS studies; V.B.P. and O.M. performed DFT studies; C.S. and V.P. analyzed data with the help of G.S. and R.V.; C.S. and V.P. wrote the paper; and all authors participated in data discussion and further analysis and commented on the manuscript.

1. S. Mitchell, A. J. Martín, G. G. Gosálbez, J. Pérez-Ramírez, The future of chemical sciences is sustainable. *Angew. Chem. Int. Ed. Engl.* **63**, e202318676 (2024).
2. J. A. Farmer, C. T. Campbell, Ceria maintains smaller metal catalyst particles by strong metal-support bonding. *Science* **329**, 933–936 (2010).
3. C. T. Campbell, C. H. F. Peden, Oxygen vacancies and catalysis on ceria surfaces. *Science* **309**, 713–714 (2005).
4. S. Joo *et al.*, Highly active dry methane reforming catalysts with boosted in situ grown Ni-Fe nanoparticles on perovskite via atomic layer deposition. *Sci. Adv.* **6**, 1573 (2020).
5. S. Li, J. Gong, Strategies for improving the performance and stability of Ni-based catalysts for reforming reactions. *Chem. Soc. Rev.* **43**, 7245–7256 (2014).
6. G. Sharma *et al.*, Pt-doped Ru nanoparticles loaded on 'black gold' plasmonic nanoreactors as air stable reduction catalysts. *Nat. Commun.* **15**, 713 (2024).
7. Z. Chen *et al.*, Splitting CO_2 into CO and O_2 by a single catalyst. *Proc. Natl. Acad. Sci. U. S. A.* **109**, 15606–15611 (2012).
8. W. C. Chueh *et al.*, High-flux solar-driven thermochemical dissociation of CO_2 and H_2O using nonstoichiometric ceria. *Science* **330**, 1797–1801 (2010).
9. J. Graciani *et al.*, Highly active copper-ceria and copper-ceria-titania catalysts for methanol synthesis from CO_2. *Science* **345**, 546–550 (2014).
10. M. A. Khoshooei *et al.*, An active, stable cubic molybdenum carbide catalyst for the high-temperature reverse water-gas shift reaction. *Science* **384**, 540–546 (2024).
11. C. Zhou *et al.*, Steering CO_2 hydrogenation toward C-C coupling to hydrocarbons using porous organic polymer/metal interfaces. *Proc. Natl. Acad. Sci. U. S. A.* **119**, e2114768119 (2022).
12. A. Tavasoli *et al.*, Enhanced hybrid photocatalytic dry reforming using a phosphated Ni-CeO_2 nanorod heterostructure. *Nat. Commun.* **14**, 1435 (2023).
13. Y. Zhu *et al.*, Environment of metal–O–Fe bonds enabling high activity in CO_2 reduction on single metal atoms and on supported nanoparticles. *J. Am. Chem. Soc.* **143**, 5540–5549 (2021).
14. D. Voiry *et al.*, Low-dimensional catalysts for hydrogen evolution and CO_2 reduction. *Nat. Rev. Chem.* **2**, 0105 (2018).
15. R. Verma *et al.*, Defects tune the acidic strength of amorphous aluminosilicates. *Nat. Commun.* **15**, 6899 (2024).
16. Y. Zhang *et al.*, Structure sensitivity of Au-TiO_2 strong metal–support interactions. *Angew. Chem. Int. Ed. Engl.* **60**, 12074–12081 (2021).
17. S. J. Tauster, S. C. Fung, Strong metal-support interactions: Occurrence among the binary oxides of groups IIA-VB. *J. Catal.* **55**, 29 (1978).
18. S. J. Tauster *et al.*, Strong interactions in supported-metal catalysts. *Science* **211**, 1121–1125 (1981).
19. T. Pu, W. Zhang, M. Zhu, Engineering heterogeneous catalysis with strong metal–support interactions: Characterization, theory and manipulation. *Angew. Chem. Int. Ed. Engl.* **62**, e202212278 (2022).
20. M. G. Willinger *et al.*, A case of strong metal–support interactions: Combining advanced microscopy and model systems to elucidate the atomic structure of interfaces. *Angew. Chem. Int. Ed. Engl.* **53**, 5998–6001 (2014).
21. P. Hu *et al.*, Electronic metal-support interactions in single-atom catalysts. *Angew. Chem. Int. Ed. Engl.* **53**, 3418–3421 (2014).
22. C. T. Campbell, Electronic perturbations. *Nat. Chem.* **4**, 597–598 (2012).
23. A. Bruix *et al.*, A new type of strong metal–support interaction and the production of H_2 through the transformation of water on Pt/CeO_2(111) and Pt/CeO_x/TiO2(110) catalysts. *J. Am. Chem. Soc.* **134**, 8968–8974 (2012).
24. C. Vogt *et al.*, Unravelling structure sensitivity in CO_2 hydrogenation over nickel. *Nat. Catal.* **1**, 127–134 (2018).
25. H. Frey *et al.*, Dynamic interplay between metal nanoparticles and oxide support under redox conditions. *Science* **376**, 982–987 (2022).
26. A. S. Hall *et al.*, Mesostructure-induced selectivity in CO_2 reduction catalysis. *J. Am. Chem. Soc.* **137**, 14834–14837 (2015).
27. R. Belgamwar *et al.*, Defects tune the strong metal–support interactions in copper supported on defected titanium dioxide catalysts for CO_2 reduction. *J. Am. Chem. Soc.* **145**, 8634–8646 (2023).
28. A. K. Mishra *et al.*, Defects in nanosilica catalytically convert CO_2 to methane without any metal and ligand. *Proc. Natl. Acad. Sci. U.S.A.* **117**, 6383–6390 (2020).
29. D. D. Beck, A. O. Bawagan, J. White, Spillover of deuterium on platinum/titanium dioxide. 2. Sequential hydrogen-deuterium exposure and effects of oxygen. *J. Phys. Chem.* **88**, 2771–2775 (1984).
30. A. S. Thill, A. S. Kilian, F. Bernardi, Key role played by metallic nanoparticles on the ceria reduction. *J. Phys. Chem. C* **121**, 25323–25332 (2017).
31. M. Xu *et al.*, Renaissance of strong metal–support interactions. *J. Am. Chem. Soc.* **146**, 2290–2307 (2024).
32. B. Zugic *et al.*, Dynamic restructuring drives catalytic activity on nanoporous gold–silver alloy catalysts. *Nat. Mater.* **16**, 558–564 (2016).
33. Y. Xie *et al.*, Double-edged sword effect of classical strong metal–support interaction in catalysts for CO_2 hydrogenation to CO, methane, and methanol. *ACS Mater. Lett.* **5**, 2629–2647 (2023).
34. Q. Fu *et al.*, Active nonmetallic Au and Pt species on ceria-based water-gas shift catalysts. *Science* **301**, 935–938 (2003).
35. M. Behrens *et al.*, The active site of methanol synthesis over Cu/ZnO/Al_2O_3 industrial catalysts. *Science* **336**, 893–897 (2012).
36. Y. Song *et al.*, Dry reforming of methane by stable Ni–Mo nanocatalysts on single-crystalline MgO. *Science* **367**, 777–781 (2020).
37. T. P. Araújo *et al.*, Flame-made ternary Pd-In_2O_3-ZrO_2 catalyst with enhanced oxygen vacancy generation for CO_2 hydrogenation to methanol. *Nat. Commun.* **13**, 5610 (2022).
38. J. Yang *et al.*, Single atomic vacancy catalysis. *ACS Nano* **13**, 9958–9964 (2019).
39. K. Jenkinson *et al.*, Direct operando visualization of metal support interactions induced by hydrogen spillover during CO_2 hydrogenation. *Adv. Mater.* **35**, 2306447 (2023).
40. M. Tang *et al.*, Facet-dependent oxidative strong metal–support interactions of palladium–TiO_2 determined by in-situ transmission electron microscopy. *Angew. Chem. Int. Ed. Engl.* **60**, 22339–22344 (2021).
41. A. Parastaev *et al.*, Boosting CO_2 hydrogenation via size-dependent metal–support interactions in cobalt/ceria-based catalysts. *Nat. Catal.* **3**, 526–533 (2020).

42. C. W. Lee *et al.*, Photochemical tuning of dynamic defects for high-performance atomically dispersed catalysts. *Nat. Mater.* **23**, 552–559 (2024).
43. J. Zhang *et al.*, Strong metal-support interactions induced by an ultrafast laser. *Nat. Commun.* **12**, 6665 (2021).
44. C. Li *et al.*, Intrinsic strain-mediated ultrathin ceria nanoantioxidant. *J. Am. Chem. Soc.* **145**, 19086–19097 (2023).
45. M. Xu *et al.*, Insights into interfacial synergistic catalysis over Ni@TiO_{2-x} catalyst toward water–gas shift reaction. *J. Am. Chem. Soc.* **140**, 11241–11251 (2018).
46. S. K. Padamati *et al.*, Transient formation and reactivity of a high-valent nickel (IV) oxido complex. *J. Am. Chem. Soc.* **139**, 8718–8724 (2017).
47. D. K. Bediako *et al.*, Structure–activity correlations in a nickel–borate oxygen evolution catalyst. *J. Am. Chem. Soc.* **134**, 6801–6809 (2012).
48. S. Qin *et al.*, Ternary nickel–tungsten–copper alloy rivals platinum for catalyzing alkaline hydrogen oxidation. *Nat. Commun.* **12**, 2686 (2021).
49. S. C. Lin *et al.*, Operando time-resolved X-ray absorption spectroscopy reveals the chemical nature enabling highly selective CO_2 reduction. *Nat. Commun.* **11**, 3525 (2020).
50. J. Yu *et al.*, Ultra-high thermal stability of sputtering reconstructed Cu-based catalysts. *Nat. Commun.* **12**, 7209 (2021).
51. C. J. Chang *et al.*, Dynamic reoxidation/reduction-driven atomic interdiffusion for highly selective CO_2 reduction toward methane. *J. Am. Chem. Soc.* **142**, 12119–12132 (2020).
52. N. J. Divins *et al.*, Operando high-pressure investigation of size-controlled CuZn catalysts for the methanol synthesis reaction. *Nat. Commun.* **12**, 1435 (2021).
53. L. Han *et al.*, Stable and efficient single-atom Zn catalyst for CO_2 reduction to CH_4. *J. Am. Chem. Soc.* **142**, 12563–12567 (2020).
54. F. Li *et al.*, Identifying the structure of Zn-N_2 active sites and structural activation. *Nat. Commun.* **10**, 2623 (2019).
55. X. Li *et al.*, Atomic-scale imaging of the defect dynamics in ceria nanowires under heating by *in-situ* aberration-corrected TEM. *Sci. China Chem.* **62**, 1704–1709 (2019).
56. B. Goris *et al.*, Three-dimensional valency mapping in ceria nanocrystals. *ACS Nano* **8**, 10878–10884 (2014).
57. W. T. Figueiredo *et al.*, Understanding the strong metal–support interaction (SMSI) effect in Cu_xNi_{1-x}/CeO_2 ($0 < x < 1$) nanoparticles for enhanced catalysis. *ACS Appl. Nano Mater.* **2**, 2559–2573 (2019).
58. D. H. Pearson, C. C. Ahn, B. Fultz, White lines and d-electron occupancies for the 3*d* and 4*d* transition metals. *Phys. Rev.* **47**, 8471–8478 (1993).
59. J. Zheng *et al.*, Ambient-pressure synthesis of ethylene glycol catalyzed by C_{60}-buffered Cu/SiO_2. *Science* **376**, 288–292 (2022).
60. A. M. Beck *et al.*, The dynamics of overlayer formation on catalyst nanoparticles and strong metal-support interaction. *Nat. Commun.* **11**, 3220 (2020).
61. K. M. Siniard *et al.*, Ultrasonication-induced strong metal-support interaction construction in water towards enhanced catalysis. *Angew. Chem. Int. Ed. Engl.* **62**, e202214322 (2023).
62. L. Chen *et al.*, Dynamic evolution of palladium single atoms on anatase titania support determines the reverse water–gas shift activity. *J. Am. Chem. Soc.* **145**, 10847–10860 (2023).
63. J. Zhao *et al.*, Exsolution–dissolution of supported metals on high-entropy $Co_3MnNiCuZnO_x$: Toward sintering-resistant catalysis. *ACS Catal.* **11**, 12247–12257 (2021).
64. R. Jin, J. Easa, C. P. O'Brien, Highly active CuO_x/SiO_2 dot core/rod shell catalysts with enhanced stability for the reverse water gas shift reaction. *ACS Appl. Mater. Interfaces* **13**, 38213–38220 (2021).
65. L. Wang *et al.*, K-promoted Co–CeO_2 catalyst for the reverse water–gas shift reaction. *Chem. Lett.* **42**, 682–683 (2013).
66. H.-X. Liu *et al.*, Partially sintered copper-ceria as excellent catalyst for the high-temperature reverse water gas shift reaction. *Nat. Commun.* **13**, 867 (2022).
67. A. M. Bahmanpour *et al.*, Cu–Al spinel as a highly active and stable catalyst for the reverse water gas shift reaction. *ACS Catal.* **9**, 6243–6251 (2019).
68. X. Zhang *et al.*, Highly dispersed copper over β-Mo_2C as an efficient and stable catalyst for the reverse water gas shift (RWGS) reaction. *ACS Catal.* **7**, 912–918 (2016).
69. H. Chen *et al.*, Dynamic phase transition of iron oxycarbide facilitated by Pt nanoparticles for promoting the reverse water gas shift reaction. *ACS Catal.* **11**, 14586–14595 (2021).
70. L. Yang *et al.*, Highly efficient Ni/CeO_2-Al_2O_3 catalysts for CO_2 upgrading via reverse water-gas shift: Effect of selected transition metal promoters. *Appl. Catal. B. Environ.* **232**, 464–471 (2018).
71. Y. Zhang *et al.*, Highly efficient Cu/CeO_2-hollow nanospheres catalyst for the reverse water-gas shift reaction: Investigation on the role of oxygen vacancies through in situ UV-Raman and DRIFTS. *Appl. Surf. Sci.* **516**, 146035 (2020).
72. H.-X. Liu *et al.*, Pt_n–O_v synergistic sites on MoO_x/γ-Mo_2N heterostructure for low-temperature reverse water–gas shift reaction. *Nat. Commun.* **13**, 5800 (2022).
73. H. Wang *et al.*, Synergistic interactions of neighboring platinum and iron atoms enhance reverse water–gas shift reaction performance. *J. Am. Chem. Soc.* **145**, 2264–2270 (2023).
74. S. Wang *et al.*, Stable Cu catalysts supported by two-dimensional SiO_2 with strong metal–support interaction. *Adv. Sci.* **9**, 2104972 (2022).
75. R. M. Belekar, Suppression of coke formation during reverse water-gas shift reaction for CO_2 conversion using highly active Ni/Al_2O_3-CeO_2 catalyst material. *Phys. Lett.* **395**, 127206 (2021).
76. B. Liang *et al.*, Promoting role of potassium in the reverse water gas shift reaction on Pt/mullite catalyst. *Catal. Today* **281**, 319–326 (2017).
77. Y. Yu *et al.*, Highly active and stable copper catalysts derived from copper silicate double-shell nanofibers with strong metal–support interactions for the RWGS reaction. *Chem. Commun.* **55**, 4178–4181 (2019).
78. D. Liu *et al.*, Efficient Ni-based catalysts for low-temperature reverse water-gas shift (RWGS) reaction. *Chem. Asian J.* **16**, 949–958 (2021).
79. R. Zhang *et al.*, Tuning reverse water gas shift and methanation reactions during CO_2 reduction on Ni catalysts via surface modification by MoO_x. *J. CO Util.* **52**, 101678 (2021).
80. E. Spennati *et al.*, CO_2 methanation vs reverse WGS activity on Co/γ-Al_2O_3 catalysts at atmospheric pressure: Effect of cobalt loading and silica addition on selectivity and stability. *Catal. Today* **420**, 114164 (2023).
81. P. Du *et al.*, Single-atom-driven dynamic carburization over Pd_1–FeO_x catalyst boosting CO_2 conversion. *Chem* **8**, 3252–3262 (2022).
82. S. Hilaire *et al.*, A comparative study of water-gas-shift reaction over ceria supported metallic catalysts. *Appl. Catal. A: Gen.* **215**, 271–278 (2001).
83. W. Jin, E. Iglesia, Isotopic and kinetic assessment of the mechanism of reactions of CH_4 with CO_2 or H_2O to form synthesis gas and carbon on nickel catalysts. *J. Catal.* **224**, 370–383 (2004).
84. R. M. Palomino *et al.*, Hydrogenation of CO_2 on ZnO/Cu(100) and ZnO/Cu(111) catalysts: Role of copper structure and metal–oxide interface in methanol synthesis. *J. Phys. Chem. B* **122**, 794–800 (2018).
85. J. Fortner, E. C. Buck, The chemistry of the light rare-earth elements as determined by electron energy loss spectroscopy. *Appl. Phys. Lett.* **68**, 3817–3819 (1996).
86. F. Xing *et al.*, Ternary platinum–cobalt–indium nanoalloy on ceria as a highly efficient catalyst for the oxidative dehydrogenation of propane using CO_2. *Nat. Catal.* **5**, 55–65 (2022).
87. J. Lu *et al.*, Coking- and sintering-resistant palladium catalysts achieved through atomic layer deposition. *Science* **335**, 1205–1208 (2012).
88. L. Chen, Q. Xu, Fewer defects, better catalysis? *Science* **367**, 737–737 (2020).
89. J. C. Matsubu *et al.*, Adsorbate-mediated strong metal–support interactions in oxide-supported Rh catalysts. *Nat. Chem.* **9**, 120–127 (2016).
90. R. Verma *et al.*, Nickel-laden dendritic plasmonic colloidosomes of black gold: Forced plasmon mediated photocatalytic CO_2 hydrogenation. *ACS Nano* **17**, 4526–4538 (2023).
91. O. Mohan *et al.*, Novel nickel-based single-atom alloy catalyst for CO_2 conversion reactions: Computational screening and reaction mechanism analysis. *J. Phys. Chem. C* **125**, 4041–4055 (2021).
92. Y. Zhou *et al.*, Asymmetric dinitrogen-coordinated nickel single-atomic sites for efficient CO_2 electroreduction. *Nat. Commun.* **14**, 3776 (2023).
93. Z. Qi *et al.*, Mechanism of methanol decomposition over single-site Pt_1/CeO_2 catalyst: A DRIFTS study. *J. Am. Chem. Soc.* **143**, 60–64 (2020).
94. S. Kattel *et al.*, Optimizing binding energies of key intermediates for CO_2 hydrogenation to methanol over oxide-supported copper. *J. Am. Chem. Soc.* **138**, 12440–12450 (2016).
95. C. Li, M. W. Kanan, CO_2 reduction at low overpotential on Cu electrodes resulting from the reduction of thick Cu_2O films. *J. Am. Chem. Soc.* **134**, 7231–7234 (2012).
96. J. Zhou *et al.*, Layer-stacked Zn with abundant corners for selective CO_2 electroreduction to CO. *ACS Appl. Energy Mater.* **6**, 2954–2961 (2023).
97. T. P. Araújo *et al.*, Low-nuclearity CuZn ensembles on $ZnZrO_x$ catalyze methanol synthesis from CO_2. *Nat. Commun.* **15**, 3101 (2024).
98. Y. Sun *et al.*, Defect engineering of ceria nanocrystals for enhanced catalysis via a high-entropy oxide strategy. *ACS Cent. Sci.* **8**, 1081–1090 (2022).
99. X. Liu, L. Sun, W. Deng, Theoretical investigation of CO_2 adsorption and dissociation on low index surfaces of transition metals. *J. Phys. Chem. C* **122**, 8306–8314 (2018).